ABSTRACT

LONG, JOSEPH PRESTON. Ultraviolet Detectors and Focal Plane Array Imagers Based on $Al_xGa_{1-x}N$ p-i-n Photodiodes. (Under the direction of Dr. Jan F. Schetzina.)

This research has been conducted in order to address the absence of effective solid-state ultraviolet (UV) detectors and imagers. Despite the wide range of advances in visible and infrared imagery, until recently there have been no semiconductor devices under development for imaging strictly in the ultraviolet region of the spectrum. Much of the difficulty in creating such devices has been due to the lack of appropriate materials; however, the development of the group III-nitrides (III-N), including materials such as GaN and AlGaN, has provided a solution to this dilemma. The $Al_xGa_{1-x}N$ based devices synthesized during this research were grown via organo-metallic vapor phase epitaxy and processed using standard photolithography, e-beam evaporation, and reactive ion etching processes. Focal plane arrays were subsequently bump bonded to silicon read-out integrated circuits (ROICs), which were then wire bonded to 84-pin leadless chip carriers. A specialized video camera and focal plane array evaluation software were used to test the imagers. The devices exhibit very low noise and very high sensitivity to ultraviolet radiation. Excellent quality UV images have been obtained for both 128x128 and 320x256 large format hybridized focal plane arrays. These new devices may find widespread usage in a number of applications that require sensitive UV detectors and UV imagers but where the cost, size, and power requirements of a photomultiplier tube cannot be justified.

ULTRAVIOLET DETECTORS AND FOCAL PLANE ARRAY IMAGERS BASED ON $Al_xGa_{1-x}N$ P-I-N PHOTODIODES

by
JOSEPH PRESTON LONG

A thesis submitted to the Graduate Faculty of
North Carolina State University
in partial fulfillment of the
requirements for the Degree of
Master of Science

PHYSICS

Raleigh

2004

APPROVED BY:

Dr. John F. Muth	Dr. Robert J. Nemanich

Dr. Jan F. Schetzina

Chair of Advisory Committee

BIOGRAPHY

Joseph Preston "J.P." Long was born to Robert Delaney and Beth Amos Long on January 9, 1979 in Durham County Hospital in Durham, North Carolina. He was raised in Charlotte, North Carolina, where he graduated from East Mecklenburg Senior High School in June of 1997. From August 1997 through May 2001, J.P. attended the University of North Carolina at Chapel Hill on a James M. Johnston scholarship, receiving Bachelor of Science degrees in both physics and mathematics in 2001. While there, he received the Daniel C. Johnson and the Paul E. Shearin awards, both presented to recognize the most outstanding physics student. In January of 2002, J.P. began graduate studies in physics under the direction of Dr. Jan Schetzina at North Carolina State University, where he remains at the present time. He plans to continue his studies there and eventually to obtain a PhD in physics.

Mr. Long's research interests include the development of nanoscale electronic and photonic materials and devices. In particular, he is concerned with low dimensional quantum structures and heterostructure devices fabricated from wide bandgap semiconductors.

When not in the laboratory, J.P. can usually be found spinning down a country road on his bicycle, training for the racing season or just enjoying the scenery and staying fit. Please, try not to run over him.

ACKNOWLEDGEMENTS

Firstly, I would like to thank my parents, Robert Delaney and Beth Amos Long, for a lifetime of encouragement and support in all aspects of my life. Their contributions to me have been and continue to be invaluable. I would also like to thank Dr. Jan Schetzina for hiring me, for guiding me through the first two years of my graduate education and for turning me from a mathematician into an engineer. (It seems that there is more to physics than just solving boundary-value problems, or so I have come to believe.) I also appreciate the assistance of Drs. John Muth and Mark Johnson, who have helped to encourage and educate me considerably throughout my graduate career. I must also acknowledge the help of the world's best laboratory technician and our resident tough-guy/biker, Joe Matthews, from whom I have learned nearly everything I know about equipment maintenance and repair and without whom this research would not have been possible. Not only did he conduct nearly all of the processing of these devices, but he also helped to develop many of the processing procedures used in their fabrication. Lastly, I would like to thank anyone and everyone else who has ever impacted my life positively in any way. I would not be where I am today if not for their contributions.

TABLE OF CONTENTS

Page

LIST OF FIGURES

1. INTRODUCTION

Over the past several decades, semiconductor photodetectors have been successfully demonstrated for use in the visible and infrared (IR) regions of the spectrum. In the far-IR (8-14 μm wavelength region of the spectrum), HgCdZnTe based devices have been the most successful, and many high-performance night vision sensory systems now rely upon this technology. In the mid-IR (2-5 μm wavelength region of the spectrum), the material choice is now InSb, and in the near-IR (0.9-1.68 μm wavelength region of the spectrum), it is InGaAs. Large-area digital imagers made from these materials have been developed and have become available commercially [1], finding applications in fields such as military surveillance, medical imagery, forensics, and defect analysis. Devices known as quantum well infrared photodetectors (QWIPs) have been created as well [2], which sense radiation ranging from the mid- to far-IR regions of the spectrum. As technology progresses, it is predicted that QWIPs eventually will reach detection frequencies beyond the far-IR, spanning into the terahertz regime [3].

Certainly the largest commercial impact has been felt through the development of silicon charged-coupled devices (CCDs). The adaptation of such devices for use in visible imagery over the past decade has yielded commercially available digital cameras employing very large area CCD arrays based on complimentary metal-oxide–semiconductor (CMOS) circuitry. The very large format (reaching over 5 million pixels at present) and the read/write capabilities of these digital imaging devices now provide an affordable and convenient alternative to traditional 35 mm film photography.

Despite the wide range of advances in visible and infrared imagery, until recently there have been no semiconductor devices under development for imaging strictly in the

ultraviolet (UV) region of the spectrum. Much of the difficulty in creating such devices has been due to the lack of appropriate materials; however, the development of the group III-nitrides (III-N), including materials such as GaN and AlGaN, has provided a solution to this dilemma.

Due to absorption by atmospheric oxygen and ozone particles, there is a region of the spectrum ranging roughly from 240-285 nm referred to as the *solar-blind* UV region [4,5]. A detector that responds to wavelengths contained exclusively within this region is termed a solar-blind detector, as it is capable of responding to radiation over a very narrow window of wavelengths that contains no interference from the sun. For the detector truly to be irresponsive to solar radiation, however, it must be located sufficiently close to the earth's surface, thereby ensuring that atmospheric absorption effects are adequately strong. The term, *visible-blind*, refers to devices that exclusively respond to UV radiation and not at all to visible light. This term includes the solar-blind window, but wavelengths outside of this region as well. Many reports of III-N based visible-blind detectors and detector arrays have been reported over the past several years [5-13].

This text describes the successful synthesis, fabrication, and testing of both visible-blind and solar-blind backside-illuminated UV photodiodes based on AlGaN p-i-n heterostructures. The general physical theory and operation of solid-state photodiodes is presented first, followed by a description of the experimental procedures employed to synthesize and characterize the various layers of specific AlGaN p-i-n heterostructures. Device processing and testing procedures are discussed as well, including experiments conducted at the Army's Night Vision Laboratories. In addition to the synthesis of discrete UV photodiodes, this text reports on the successful development of large-format UV imaging

arrays, including 128x128 and 320x256 AlGaN p-i-n photodiodes designed to sense radiation in the 300-365 nm and 250-285 nm portions of the UV spectral region. Details of the device synthesis and processing are discussed, including flip-chip bonding procedures to silicon read-out integrated circuits (ROICs). Also presented are the spectral responsivities R_λ and R_0A measurements from which photodiode detectivities D* were estimated. Finally, a selection of images obtained using the large-format UV photodiode arrays is presented.

2. PHYSICS AND OPERATION OF SEMICONDUCTOR PHOTODIODES

Photodiodes and photodiode arrays possess many advantages over more traditional photodetectors, such as photomultiplier (PM) tubes. The extremely small size and light weight of photodiodes make them highly portable and able to be integrated easily into microelectronic and fiber-optic systems. Photodiodes are also extremely fast and responsive, with relatively little noise, in addition to providing a linear output over a large range of incident optical powers. Possibly among the greatest advantages of photodiodes, however, are their low cost and small voltage and power requirements as compared to PM tubes and other such devices.

The current versus voltage (I-V) characteristic of a photodiode behaves as any typical p-n junction, following the standard diode equation [14]

$$I(V) = I_0\left(e^{\frac{qV}{kT}} - 1\right) \tag{1}$$

When light is exposed to the photodiode, this equation must be modified due to the generation of additional carriers within the device. The I-V relationship in this case is given by [14]

$$I(V) = I_0\left(e^{\frac{qV}{kT}} - 1\right) - qAG\left(L_p + L_n\right) \tag{2}$$

in which q is the electronic charge, A is the device area, G is the carrier generation rate, and L_p and L_n are the diffusion lengths of the minority holes and electrons, respectively. The I-V characteristics of a typical photodiode are shown below in Figures [1,2]. In general, photo-diodes are operated under reverse bias. This is illustrated by quadrant 3 of Figure [2] and is

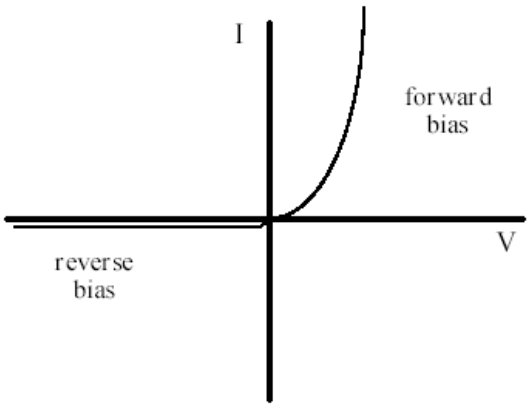

Figure 1: I-V characteristic of a typical photodiode under zero illumination. (After Kolbas.)

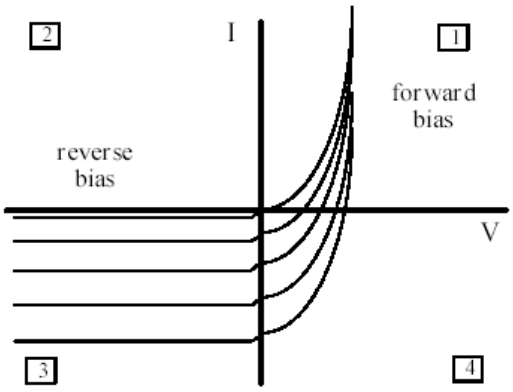

Figure 2: I-V characteristics of a typical photodiode under differing illumination levels. The four quadrants of photodiode operation are illustrated as well. (After Kolbas.)

typically referred to as the photodiode mode of operation. Quadrant 4 of Figure [2] is called the photovoltaic mode of operation.

To better understand the way in which a photodiode converts radiation into an electric signal, one must first address the process of absorption. As light strikes the photodiode, the device may absorb some of the incident radiation. This absorption is particularly significant for the case of incident radiation possessing energies larger than the band gap (E_g) of a direct gap semiconductor material. The process responsible for this particular absorption process is photon-electron scattering. As a photon (with energy $h\nu > E_g$) enters the device, it is likely to collide with an electron in the valence band of the semiconductor material. This collision transfers energy from the photon to the electron, providing the electron with enough energy to be promoted into the conduction band. This, in turn, creates a hole in the valence band. Figure [3] shows this process schematically.

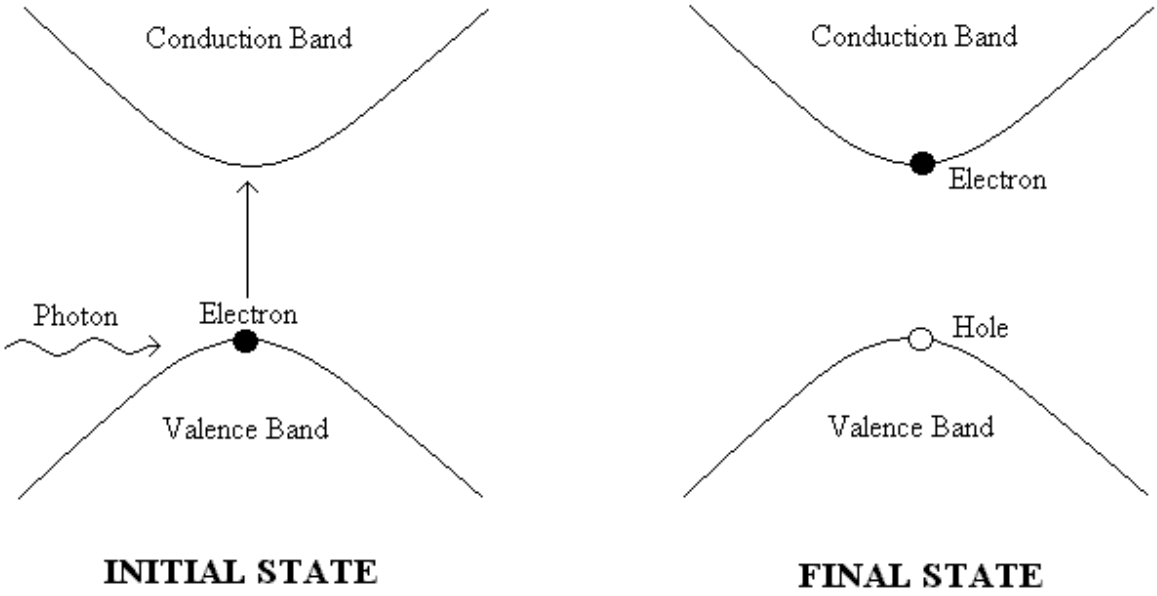

Figure 3: Schematic representation of the absorption process due to photon-electron scattering in a direct band gap semiconductor.

The absorption process generates electrons and holes (photocarriers), but this occurs in any slab of direct semiconductor material. The process by which these photocarriers exit the device is also of much importance. Consider Figure [4], depicting a cross-section of a typical p-n junction. The depletion width, W, signifies the space charge region of the p-n junction, and as before, L_p and L_n signify the diffusion lengths of the minority holes and electrons, respectively. Suppose that the absorption of a photon occurs within the space charge region of the p-n junction, generating an electron-hole pair. In this region of the device, there exists a very strong electric field, pointing from the n-type region to the p-type region. Because of this built-in field, the electron will be swept out of the space charge region into the n-type side, and the hole will be swept into the p-type side. This process is known as carrier drift. If the absorption occurs within L_n of the depletion region on the

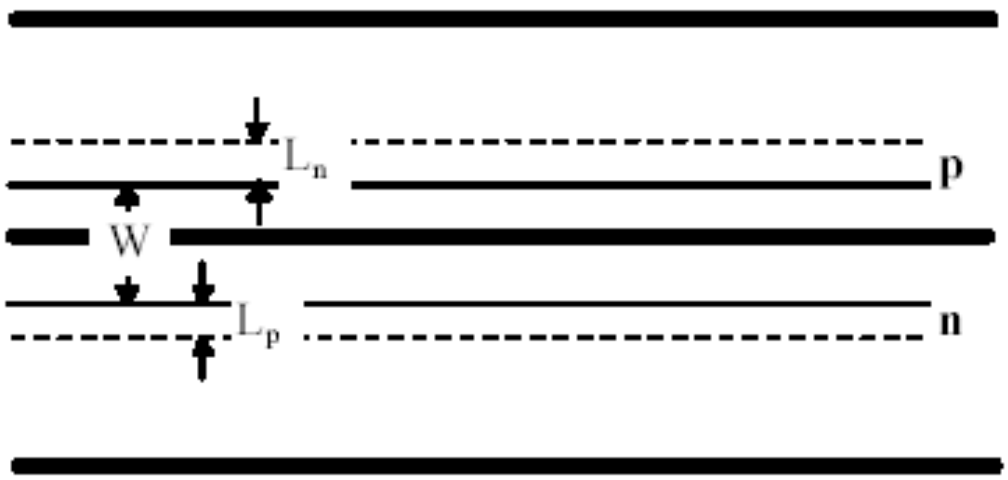

Figure 4: A cross-section of a typical p-n junction. (After Kolbas.)

p-type side of the junction, the electron may still diffuse into the space charge region before recombining and be swept out to the n-type region. The analogous process may occur for holes if the absorption process occurs within L_p of the depletion region on the n-type side of the junction. This process is called carrier diffusion.

While under illumination, carrier diffusion and drift should be the two primary components of the total current within the device. In fact, they are generally the only significant components to the signal current. Since only absorption occurring within these drift and diffusion regions produces signal current, it is desirable to control the thickness of these areas. Unfortunately, one has little control over the size of the diffusion region; this is a property of the semiconductor material. The width of the diffusion region is given by the diffusion length $L=(D\tau)^{1/2}$ [15], in which D and τ are, respectively, the diffusion coefficient and recombination lifetime of the carriers. These quantities can be altered only by changing the material comprising the photodiode; however, this can affect the overall properties of the device quite drastically.

The size of the depletion region, nevertheless, can be tuned by two principle means. In general, the width of the depletion region in a p-n junction is given by the equation [14]

$$W = \sqrt{\frac{2\varepsilon\left(V_{bi} + V_{applied}\right)}{q}\left(\frac{1}{N_a} + \frac{1}{N_d}\right)} \tag{3}$$

in which ε is the dielectric constant of the semiconductor material, q is the electronic charge, N_a and N_d are the accepter and donor densities, respectively, and V_{bi} and $V_{applied}$ are, respectively, the intrinsic potential and the reverse bias applied across the depletion region. One way to increase the width of the depletion region simply is to change the potential applied to the device. By increasing the external (reverse) bias on the photodiode, one increases $V_{applied}$ and thereby expands the size of the depletion region. In an analogous manner, the depletion region can be made smaller by decreasing the reverse bias on the device.

The second primary manner by which the size of the depletion region can be altered is by adding an intrinsic (un-doped) layer between the n- and p-type layers, creating a so-called p-i-n photodiode. In an ordinary, unbiased p-n junction, the size of the depletion region is fixed by the intrinsic (or built-in) potential and the Debye length. In a p-i-n photodiode, however, the space charge region is allowed to expand throughout the entire intrinsic layer without such limitations. This is a very common way to increase the size of the depletion region in a device.

While an increase in the size of the depletion region can increase a device's detection efficiency, a larger detection region is not always beneficial. As the size of the detection area increases, the time carriers require to traverse and exit the device increases, slowing the

response speed of the detector. Much care is essential in the device design process in order to optimize the detection efficiency and the response speed.

3. PROPERTIES OF SEMICONDUCTOR PHOTODIODES

Consider a p-n junction or p-i-n junction photodiode operating in the photovoltaic mode at zero bias [12]. The responsivity R_λ of the device is defined as the ratio of the output current i_p to the diode illumination power P_λ at a given wavelength. That is,

$$R_\lambda = \frac{i_p}{P_\lambda} = \frac{q\eta}{h\upsilon} = \left(\frac{q\eta}{hc}\right)\lambda \tag{4}$$

in which q is the electronic charge, η is the quantum efficiency, h is Planck's constant, ν is the radiation frequency, and λ is the radiation wavelength. The quantum efficiency, η, simply represents the average number of electron-hole pairs generated by each incident photon. Large responsivity values are desirable in photodetectors because this means large output signals can be attained from rather modest optical inputs. In the UV portion of the spectrum, however, even the ideal responsivities (η=1) are rather small, ranging from R_λ = 0.294 A/W at 365 nm to R_λ = 0.161 A/W at 200 nm. This places physical limitations on the performance of visible- and solar-blind photodiodes.

Another important figure of merit for a diode detector is the R_0A product, where R_0 is the dynamic resistance of the diode at zero bias, and A is the detector area. A large R_0A product is a necessary requirement for the detector to have a large detectivity D* meaning that it is able to produce a measurable signal current at very low radiation levels. Figure [5] shows the spectral detectivity values for a number of different commercially-available detectors [17] that operate at wavelengths ranging from 0.2 μm (UV) to 12 μm (far-IR). It is clear from the Figure that IR detectors display D* values of 10^7 - 10^{10} (cm $Hz^{1/2}W^{-1}$), depending on the type of detector, the operating temperature, and the wavelength region for

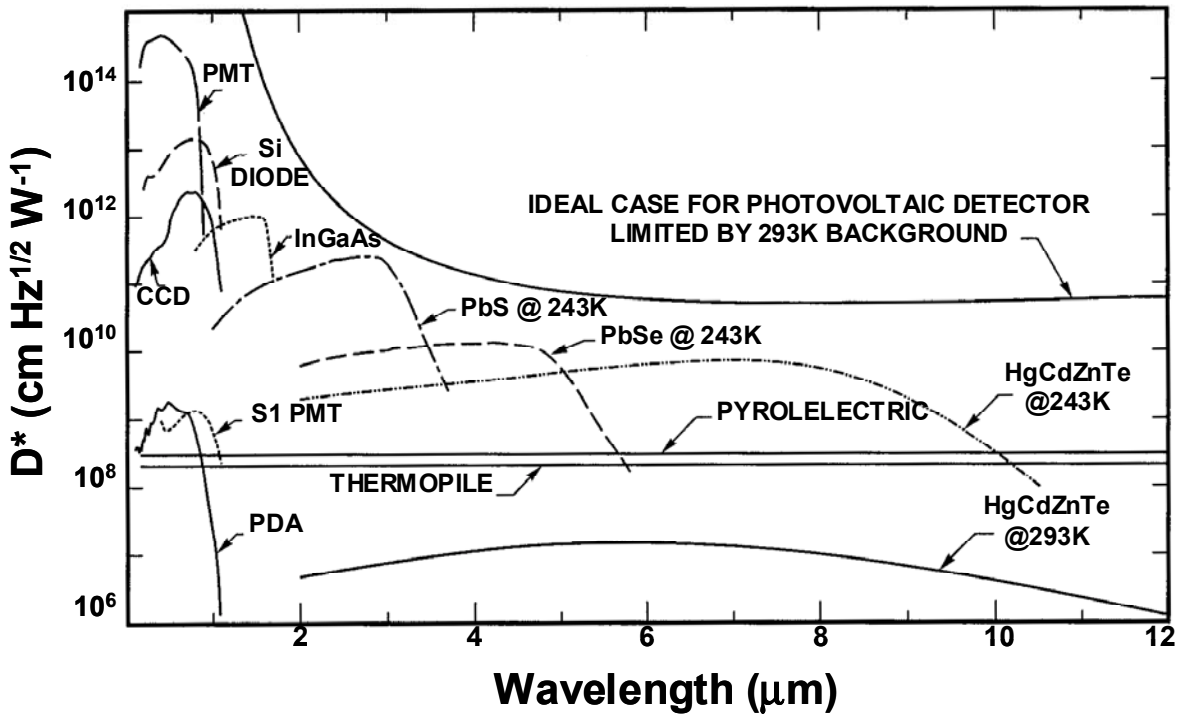

Figure 5: Detectivity D* versus wavelength for selected photodetectors.

which it is designed. Detectors operating at shorter wavelengths generally display larger D* values, ranging up to 4 x 10^{14} (cm $Hz^{1/2}W^{-1}$) for a photomultiplier tube (PMT) operating at about 300 nm.

Figure [5] also shows the curve for an ideal photovoltaic detector, limited only by a 293 K thermal background radiation source. This background radiation is due to the earth itself, and is unavoidable for devices operating at or near its surface. A detector displaying D* values that lie along this line is said to be background-limited. Such a detector also may be referred to as being a BLIP-limited detector, or simply as being BLIP-limited [16]. (BLIP is an acronym for Background-Limited Infrared Photodetector.) These devices have the highest possible D* values for a given wavelength when exposed to the earth's thermal radiation field. Note from Figure [5] that D* values for a BLIP-limited detector become

extremely large as the wavelength decreases into the UV. This is because the spectrum of a 293 K black body contains virtually no UV radiation; therefore, a tremendously sensitive photodetector is required in order to sense this near-zero UV background radiation from the earth.

The spectral detectivity D* of a photodiode detector may be expressed as [16]

$$D^* = \frac{q\eta}{h\upsilon}\left(\frac{4kT}{R_0A} + 2q^2\eta\Phi_b\right)^{-\frac{1}{2}} \tag{5}$$

in which k is Boltzmann's constant, T is the absolute temperature of the photodetector, Φ_b is the background radiation to which the detector is exposed, and the remaining quantities are as before. The first term ($4kT/R_0A$) arises from thermal noise sources within the detector, and the second term ($2q^2\eta\Phi_b$) is due to any background radiation. If the detector is limited by thermal noise, meaning that the thermal noise signal far exceeds the signal induced by background radiation, then the detectivity becomes

$$D^* = \frac{q\eta}{h\upsilon}\sqrt{\left(\frac{R_0A}{4kT}\right)} \tag{6}$$

Note that the detectivity is directly proportional to $(R_0A)^{1/2}$ when the detector is noise-limited. Thus, to develop very sensitive detectors it is essential that the detector noise sources be minimized so that R_0A is large. In the case of III-N materials, the extremely large density of dislocations represents a significant source of noise; therefore, dislocation reduction is expected have a very positive effect on the detectivity of nitride-based photodiodes.

If the second term in brackets of equation (5) above dominates, then the background signal determines D*. In this case, the detector is BLIP-limited, and D^* may be expressed as

$$D^*_{BLIP} = \frac{1}{h\upsilon}\sqrt{\left(\frac{\eta}{2\Phi_b}\right)} \tag{7}$$

The detectivity D* also may be expressed in terms of the detector noise equivalent power (NEP). The NEP is a quantity that signifies the rms optical power of an input signal required to generate the noise level present in a detector. In other words, the NEP is the rms optical input required to generate a signal-to-noise ratio of unity over a bandwidth of 1 Hz. With this definition, the detectivity also can be expressed as [16]

$$D^* = \frac{\sqrt{A\Delta f}}{NEP} \tag{8}$$

in which A is the device area, and Δf is the bandwidth of the detector.

4. EXPERIMENT DESCRIPTION

4.1 Photodiode Device Structures

Photodiode device structures were prepared by organo-metallic vapor phase epitaxy (OMVPE), using a low-pressure, vertical-flow reactor that employs high speed substrate rotation during film growth. The photodiode structures were deposited onto double-side polished 50 mm diameter c-plane sapphire substrates. A thin aluminum nitride (AlN) buffer layer was first deposited at 500-650 ^{o}C to initiate growth, and all subsequent layers were grown at 1050-1080 ^{o}C.

A schematic of a representative photodiode structure employed in the present work, which is designed to respond to UV radiation in the 320-365 nm wavelength range, is shown in Figure [6]. The low-temperature AlN nucleation layer is first deposited (not shown), followed by a 1.0 μm thick n-type silicon doped $Al_{0.23}Ga_{0.77}N$ base layer. An un-doped 0.2 μm thick GaN layer is then deposited, followed by a 0.5 μm thick p-type magnesium-doped GaN layer to complete the p-i-n heterostructure.

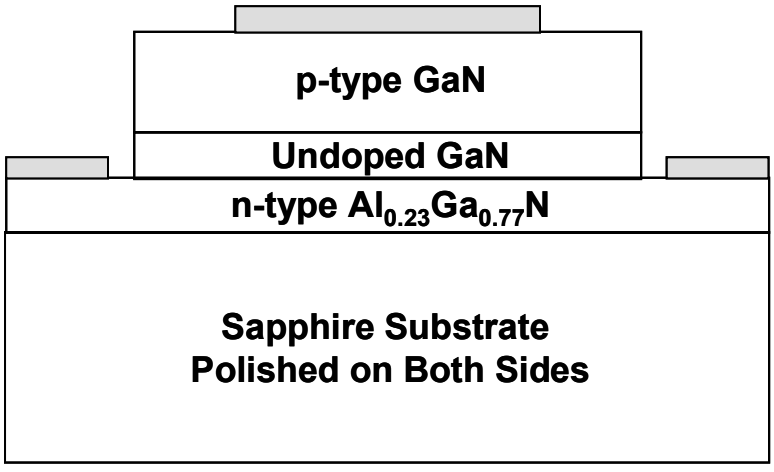

Figure 6: Stacking sequence of a visible-blind photodiode designed to detect radiation in the 320-365 nm wavelength range.

Note that this device structure is designed for illumination to occur through the substrate. At wavelengths shorter than 320 nm, the incoming radiation is absorbed in the thick AlGaN base layer (23% Al), and the junction is not illuminated. Similarly, the diode does not respond to wavelengths greater than 365 nm since this corresponds to the optical absorption edge of GaN at room temperature. Though it will not be absorbed by the AlGaN layer, any radiation at wavelengths larger than this will not have energies sufficient to excite electron-hole pairs within the device. Figure [7] shows the basic band diagram of this device, which illustrates these concepts.

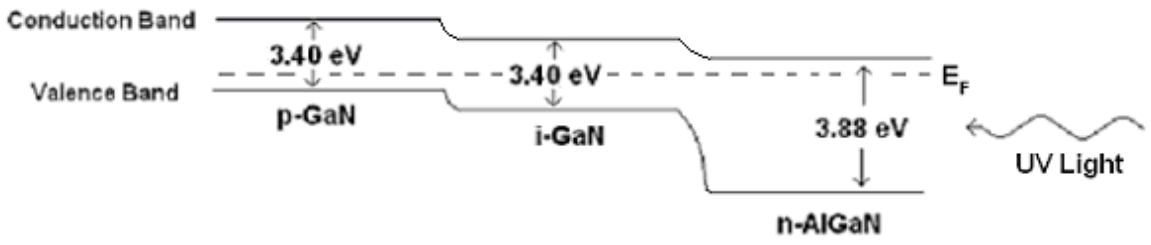

Figure 7: Band diagram for a visible-blind photodiode designed to detect radiation in the range of 320-365 nm.

Using the basic device structure shown in Figure [6], it is possible to tailor the responsivity window of the UV detector by adjusting the aluminum mole fraction present in each of the three layers. This can be done because the band gap of $Al_xGa_{1-x}N$ varies as given by the empirical equation [18]

$$E_g(x) = 6.2x + 3.4(1-x) - 0.25x(1-x) \qquad (9)$$

Thus, it is possible to synthesize detectors that sense different UV spectral regions. For example, the diode structure shown in Figure [8] is designed to sense UV radiation in the 240-285 nm solar-blind spectral region. Figure [9] shows the corresponding band diagram.

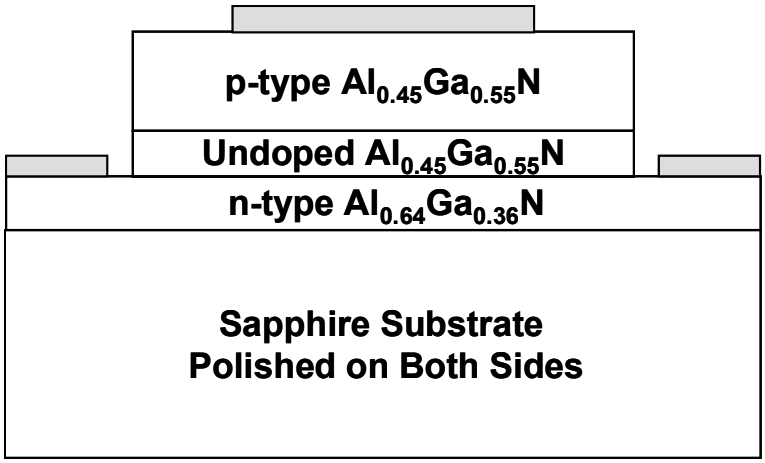

Figure 8: Stacking sequence of a solar-blind photodiode designed to detect radiation in the 240-285 nm wavelength range.

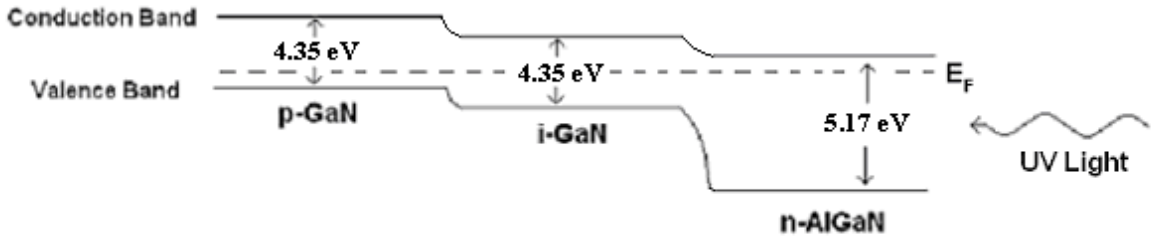

Figure 9: Band diagram for a solar-blind photodiode designed to detect radiation in the range of 240-285 nm.

In order to optimize these photodiode structures, a series of samples were grown under various combinations of growth temperatures, growth rates, and gas flow rates. For example, for the solar-blind diode structure, the n-type $Al_{0.64}Ga_{0.36}N$:Si was first optimized.

Capacitance-voltage (C-V), optical absorption, and cathodoluminescence (CL) measurements were employed in this optimization procedure. The un-doped $Al_{0.45}Ga_{0.55}N$ active layer and p-type magnesium doped $Al_{0.47}Ga_{0.53}N$:Mg top layer of the device structure were then optimized with the aid of optical absorption and cathodoluminescence measurements.

4.2 Device Processing

All device processing was completed using standard semiconductor processing techniques, which included photolithography using appropriately-designed masks, reactive ion etching to define mesa structures, and metallizations to provide ohmic contacts to the n-type and p-type layers of the devices. Boron trichloride (BCl_3) was employed in the reactive ion etching chamber, using photolithographically defined nickel masks to etch the photodiode mesas. Etch rates of roughly 17.5 nm/sec were obtained using BCl_3 flow rates of 35 sccm, a chamber pressure of 30 mTorr, and an RF power level of 100 W. The discrete photodiodes used for responsivity and R_0A measurements were defined by 200 μm x 200 μm mesas. The 128 x 128 photodiode arrays employed 32 μm x 32 μm mesa diodes on a 38 μm pitch. The larger 320 x 256 photodiode arrays consisted of 24 μm x 24 μm mesa diodes on a 30 μm pitch. Ni/Au and Ti/Al metallizations were employed to obtain p-type and n-type ohmic contacts, respectively. These contacts were created via a deposition, employing an electron beam evaporation system, followed by subsequent annealing at 600-700 ^{o}C.

The UV photodiode arrays were hybridized to silicon readout integrated circuits (ROICs) using an indium bump bonding procedure. Indigo Systems Corporation's 9802 and 9809 ROICs were employed for the hybridization of the 128x128 and 320x256 photodiode arrays, respectively. In this flip-chip bonding procedure, photoresist was used to define 18 μm circular vias at all of the p-contact and n-contact points on the photodiode array, as well

as at the corresponding metal pads of the silicon ROIC. An ultra-high vacuum (UHV) deposition system, which employs effusion cells, was then used to precisely deposit a uniform array of indium bumps having thickness 5-10 μm onto the photodiode array and onto the silicon ROIC. The photodiode array was then hybridized to the silicon ROIC using an RD Automation model M8-G flip-chip aligner bonder. The hybridized focal plane array (FPA) was then cemented onto an 84-pin leadless chip carrier (LCC). Outputs from the ROIC were wire-bonded to the LCC using gold wires. The completed UV camera chip was then inserted into a matching 84-pin socket located on a circuit board in the FPA evaluation and demonstration camera system, manufactured by the SE-IR Corporation. The SE-IR camera system employs a UV-compatible fused quartz focusing lens, along with hardware and software for reading out, displaying, and storing UV images from the 128x128 and 320x256 FPAs as single snap-shots or as digital movies acquired at selected frame rates.

4.3 Device Testing

In order to characterize individual devices, spectral responsivity R_λ measurements were made on selected photodiode samples. In these experiments, a xenon lamp was employed as a UV source, and the UV illumination wavelengths were selected by a monochromator. The output of the monochromator was calibrated using a special UV-enhanced silicon photodiode with a known responsivity profile. Noise reduction was performed by placing an optical chopper in the path of the beam and using a lock-in amplifier, set to respond to the chopper's frequency. The spectral responsivity R_λ of the photodiodes was then calculated from the measured photocurrent through the aid of Equation (4).

In addition, the room-temperature dynamic photodiode resistance at zero-bias R_0 was measured for selected devices using a shielded, low-noise enclosure and shielded probe tips. These measurements were combined with the device area A to obtain the R_0A product, a well-known figure of merit for photodiodes. The R_0A product was then used in order to obtain an estimate of the noise-limited detector detectivity D* by using Equation (6).

Testing of both 128x128 and 320x256 FPA devices was carried out with the aid of the SE-IR computer-controlled digital camera. Alphanumeric and geometric objects were recorded with the 128x128 and 320x256 UV digital camera chips by using templates that were back-illuminated with a UV lamp, as shown in Figure [10]. For the visible-blind (300-365 nm)

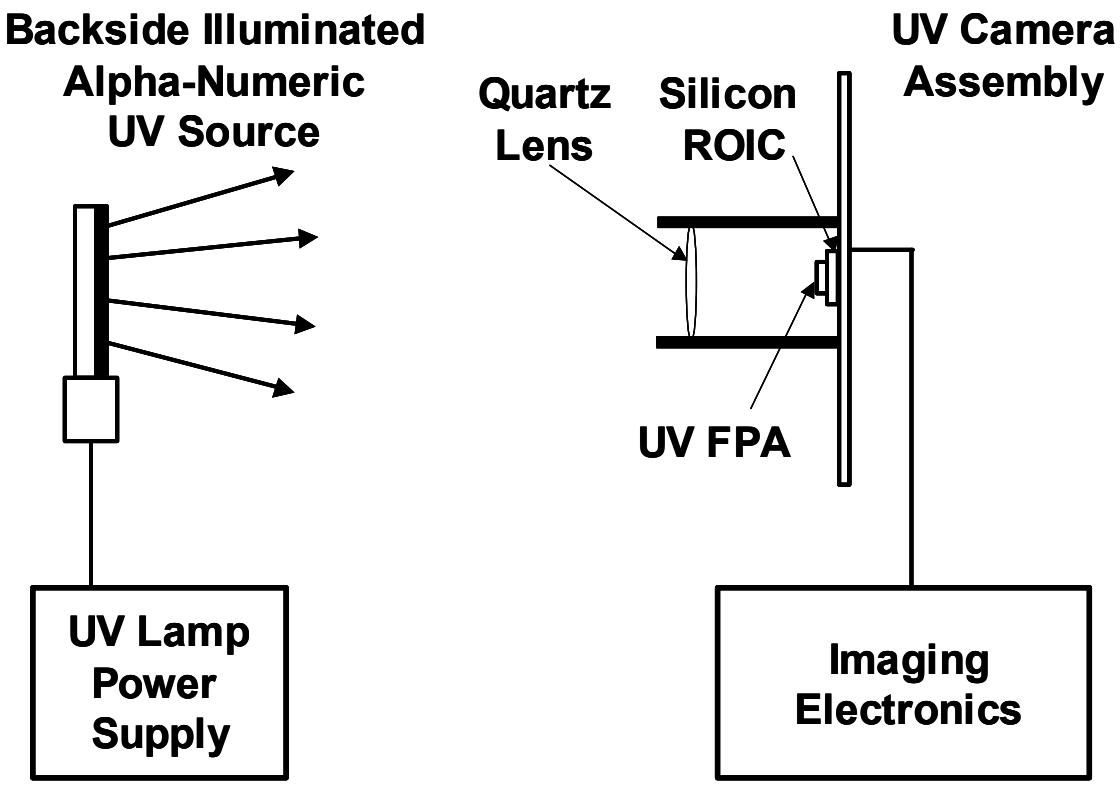

Figure 10: A schematic representation of the visible-blind FPA evaluation experiments. Using a UV lamp to back-illuminate templates, the images were recorded via the digital SE-IR camera, outfitted with a visible-blind UV FPA.

FPAs, templates were constructed using ink jet printer transparency sheets onto which were printed objects of interest, and a UV lamp producing 300-370 nm radiation was employed to back-illuminated these objects. Images of two UV sources, an oxyacetylene torch and a tungsten inert gas (TIG) arc welder, were also obtained through direct imaging by the SE-IR digital camera. For the solar-blind (240-285 nm) FPAs, brass templates with milled-out alpha-numeric patterns were employed. These were back-illuminated with the 253.6 nm output from a mercury (argon) lamp.

The SE-IR digital camera was designed originally as an FPA evaluation tool, not simply as an imager. As such, it is equipped with a number of signal processing features. These include algorithms for image corrections and the statistical analysis of pixels, in addition to a variety of image display features. Algorithms for bad pixel filtering exist, as do features such as calculating diode voltage histograms, adjusting video gain and offset, and displaying vertical line scan profiles. All of these features are built into the SE-IR camera FPA evaluation software. Most of these tools can be used for the entire array or for any rectangular subset of it, including individual pixels.

The diode voltage histogram is a particularly useful tool. This can be used in order to calculate diode current statistics and, ultimately, to estimate the NEP and D* statistics of the FPA from the independently determined discrete responsivities of the diodes. As light is detected by the photodiodes, they begin to build up potentials V due to the electron-hole pairs being generated within them. Of course, these potentials are also built up on the ROIC pixels to which the diodes are bonded. At the end of each signal collection period, defined by the camera's integration time Δt these signals are buffered and read out by the ROIC and SE-IR

camera electronics. Knowing the voltage statistics of the FPA from the evaluation software, the FPA current statistics can be calculated by using

$$I = C\left(\frac{V}{\Delta t}\right) \tag{10}$$

in which V is the diode voltage built up over an integration time Δt and C is the capacitance of the ROIC pixels listed in the technical data provided by the manufacturer. This technique is useful for obtaining current profiles both with and without any uniform device illumination. The currents obtained under uniform illumination are referred to as signal currents.

The noise present in the device under zero illumination is called the dark current, I_{DK}. Let the voltage built up on a diode under no illumination be called ΔV. Then, from Equation (10) we have the relationship

$$I_{DK} = C\left(\frac{\Delta V}{\Delta t}\right) \tag{11}$$

This permits the calculation of an FPA dark current statistics by using the FPA voltage statistics. Recall that Equation (4) relates the responsivity R_λ, optical power P_λ, and output current i_p of a photodiode by $R_\lambda = i_p/P_\lambda$. From this equation and the definition of NEP given at the end of Section 3, we see that [16]

$$NEP = \frac{I_{DK}}{R_\lambda} = \frac{C}{R_\lambda}\left(\frac{\Delta V}{\Delta t}\right) \tag{12}$$

This equation provides an estimate of the FPA's noise equivalent power statistics by using the independently determined average responsivity of the diodes in the array. Finally, from Equation (8), one can obtain an estimate of the FPA's detectivity statistics through the aid of the equation

$$D^* = \frac{\sqrt{A\Delta f}}{NEP} = \frac{R_\lambda \Delta t \sqrt{A\Delta f}}{C\Delta V} \tag{13}$$

in which A is the device area, and Δf is the camera's frame rate.

While the acquisition of FPA statistics is a very useful evaluation tool, it is ultimately the images taken with the FPA and SE-IR camera which demonstrate how well the device array performs. Without employing any image correction algorithms, standard imaging with the SE-IR camera is rather straight-forward. The collection time for each frame can be adjusted by changing the frame rate or integration time. Also, video gain and offset features can be adjusted in order to modify signals sent to the camera. These adjustments ensure that the camera's input signals are within the appropriate range for the analog to digital (A/D) converter. If signals are too high, saturation occurs; if signals are too low, no signal at all is registered. In order for A/D conversion and signal processing to be as effective as possible, input signals should be distributed throughout the entire A/D converter input range. Once these signals are corrected appropriately, the digital outputs can be modified by using an additional gain and offset, routinely referred to as the contrast and brightness, respectively. For an uncorrected image taken from the FPA, frame rate, video gain and offset, and brightness and contrast are by far the most critical parameters.

In addition to these basic signal processing features, there are also a number of algorithms which can be used to modify the output signals to correct for non-uniformities in the images. Perhaps the simplest of these is the image subtraction feature, which is quite common among many electronic devices equipped with imaging arrays. This function performs the real-time subtraction of a reference image from the live video images being acquired, permitting the operator to touch up single points or to correct for larger non-

uniformities and drift in the images. This type of filtering is also referred to as a single-point non-uniformity correction (NUC).

Another signal processing feature, which corrects for bad or unresponsive pixels (diodes), is also present in the SE-IR camera software. This data filter is the so-called two-point non-uniformity correction, which compensates for both gain and offset differences in individual pixels. It, like the single-point NUC correction, employs a numerical algorithm in order to modify a user-defined bad pixel file. In the case of the single-point NUC correction, the bad pixel file (or reference image) is simply subtracted from the live image as it updates. In order perform a two-point NUC correction, however, two reference levels are required. A low-level uniform illumination source is used to obtain the first reference level, and a higher-intensity uniform light source is then used to define the second reference level.

In practice, this is done by removing the camera lens so that the diode array is uniformly illuminated by the UV light source appropriate for the FPA under consideration. A neutral density filter is then placed between the source and the detector array. The optical densities of the filters required for this process depend on the array and source properties; they are determined empirically by observing the analog signal levels at the camera's input. This method is analogous to the process by which one makes adjustments to the video gain. In this case, however, the gain is adjusted by the neutral density filter and not by the camera's electronics. Typically, low-level references were set so that the average response signals were somewhere between 10-20% of the A/D converter's input range; high-level references were generally set so that the average response signals were somewhere between 80-90% of this range. Pixels which produce signals below or above the specified ranges of tolerance are considered bad and are stored in the bad pixel file to be modified by the two-

point NUC algorithm. To make the bad pixel definition more accurate, multiple frames can be averaged while collecting the reference levels.

The actual numerical algorithm employed by the two-point NUC is

$$X_i' = \frac{T_g G_i}{32768}\left(2X_i + B_i\right) \tag{14}$$

in which X'_i is the corrected signal for pixel i, T_g is the target gain (in general <1.0), G_i is the gain coefficient for pixel i, X_i is the signal of pixel i from the A/D converter, and B_i is the offset of pixel i. The target gain, T_g, is unity if no correction is to be performed. The level of unity gain in the quantity, G_i is 16284 A/D counts. In order to obtain the optimal two-point NUC, it is necessary not only to find the appropriate neutral density filters, but also to use the best values for the variables in Equation (14). Overall, the process for determining all of these parameters is quite empirical and can be time-consuming; it is more of an art than a science. Fortunately, this needs only to be done once for each FPA, and the corrections, in general, can improve the images significantly.

Another useful feature of the SE-IR FPA evaluation software is the option of displaying the spectral band ratios, which permits the user to conduct vertical line scans of the FPA. First, two rectangular subsets of the FPA, having equal area and being aligned both horizontally and vertically, are defined by the user. The signals are then averaged over each vertical column of diodes contained in these regions. Finally, the output is in the form of real-time histograms of the averaged column signals in both regions, as well as of their difference. This is similar in many ways to functions performed by the hardware in spectrometers.

5. RESULTS AND DISCUSSION

5.1 Discrete Diode Characteristics

Figure [11] shows a plot of the room temperature spectral responsivity R_λ versus wavelength for a selected visible-blind UV photodiode sample. The responsivity reaches its

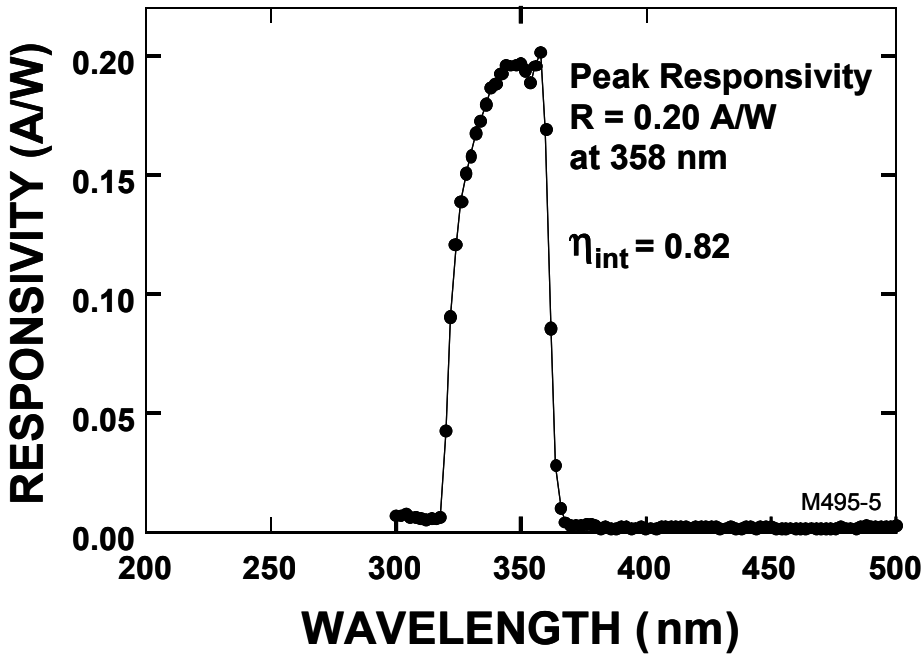

Figure 11: Selected data showing the responsivity versus wavelength for a visible-blind UV photodiode.

maximum value of 0.2 A/W at a wavelength of 358 nm. According to Equation (4), this corresponds to an external quantum efficiency of 70%. Assuming the reflection losses at the air-sapphire, sapphire-AlGaN, and AlGaN-GaN interfaces is about 12 % [7], one obtains an internal quantum efficiency of about 82% for this device. The responsivity remains fairly constant until about 320 nm, at which point it begins to decrease rapidly due to optical absorption occurring in the $Al_{0.20}Ga_{0.80}N$ base layer of the device. The R_0A value for this discrete photodiode was determined to be 1.5 x 10^9 Ω–cm^2, and its D* value was determined

to be 6.1 x 10^{13} cm $Hz^{1/2}W^{-1}$. This D* value, obtained at room temperature, is one of the largest D* values ever obtained for any semiconductor photodetector operating at any temperature and at any wavelength. As illustrated by Figure [5], this D* value approaches that of commercially available UV photomultiplier tubes (PMTs). Thus, with continued development, the nitride-based UV photodiodes may provide a solid state alternative to PMTs in the UV spectral region.

Figure [12] shows a responsivity spectrum obtained for a representative solar-blind UV photodiode at zero bias (photovoltaic mode). The solar-blind device exhibits a very

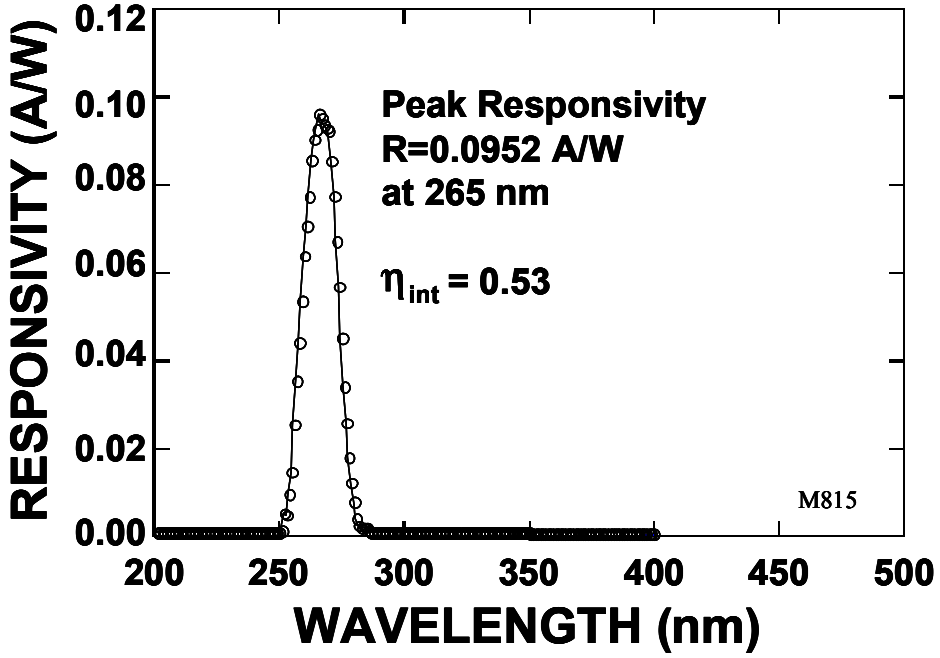

Figure 12: Selected data showing the responsivity versus wavelength for a solar-blind UV photodiode.

narrow UV spectral responsivity band, peaked at 265 nm and well within the 240-285 nm solar-blind window. The full width at half the maximum value (FWHM) is 21 nm, and the

maximum responsivity of 0.0952 A/W (at 265 nm) corresponds to an internal quantum efficiency of 53%. The responsivity falls off sharply at wavelengths greater than 285 nm since this device is transparent in this wavelength region. Similarly, the responsivity becomes very small at wavelengths shorter than 250 nm due to absorption occurring in the n-type $Al_{0.64}Ga_{0.36}N$:Si base layer of the device. Hence, the AlGaN heterostructure that has been developed produces a narrow solar-blind responsivity band, without requiring any external filters. The R_0A value for this discrete solar-blind photodiode was determined to be 2.0×10^9 Ω–cm^2, which corresponds to a D* value of 3.3×10^{13} cm Hz$^{1/2}$W^{-1} at 265 nm.

5.2 Initial 128x128 and 320x256 Visible-Blind Focal Plane Arrays

Images of UV radiation obtained using a 128x128 visible-blind focal plane array are displayed in Figures [13-16]. In Figure [13], UV images of several geometric shapes are

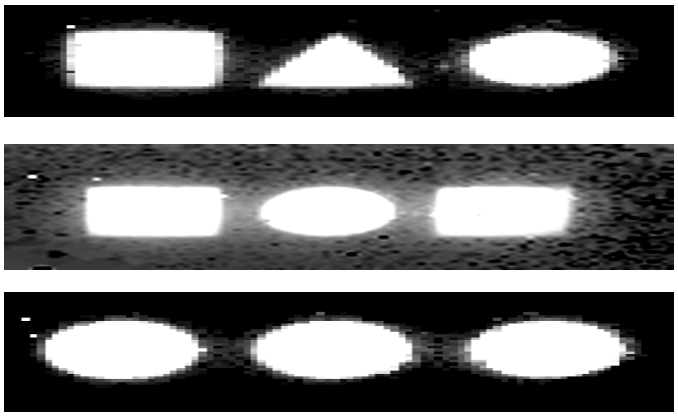

Figure 13: Images of various geometric shapes generated by a 128x128 visible-blind FPA and the SE-IR camera. Note the high pixel yield (>95%).

shown. These images illustrate the high pixel yield (greater than 95%) that has been achieved for this type of UV digital imager.

Figure [14] shows a visible image of a tungsten-inert-gas (TIG) arc welder, as well as an image of its UV emission (320-365 nm). The UV image shown here was obtained using a

Figure 14: A visible image of a tungsten-inert-gas (TIG) arc welder (left), as well as an image of its UV emission in the range of 320-365 nm (right).

128x128 FPA. In order to obtain this image, it was necessary to use a neutral density filter (#4) in front of the SE-IR camera. The filter served to reduce the intensity of the UV emission from the arc welder, thereby avoiding pixel saturation. Figure [15] shows similar

Figure 15: A visible image of an oxy-acetalene torch (left), as well as an image of its UV emission (right).

UV imagery (300-365 nm) obtained from an oxy-acetylene torch. It should be noted that all of the UV images were obtained at room temperature and under standard room lighting. Note, however, that the 128x128 FPA is entirely blind to all visible radiation. Figure [16] shows visual images, as well as UV images taken with a 128x128 visible-blind FPA. The UV images were obtained by using the template technique discussed previously.

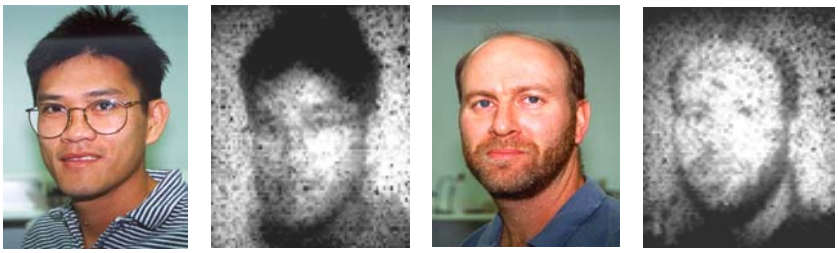

(a) (b) (c) (d)

Figure 16: Visual (a,c) and UV (b,d) images of two individuals taken with a 128x128 visible-blind FPA.

UV images obtained using one of the initial 320x256 visible-blind nitride focal plane arrays are shown in Figure [17]. It is seen from this figure that the image resolution is substantially improved over the 128x128 visible-blind FPA; however, a fairly large number of pixels (more than 15%) are inactive.

(a) (b) (c) (d)

Figure 17: Visual (a,c) and UV (b,d) images of two individuals taken with a 320x256 visible-blind FPA.

5.3 320x256 Solar-Blind Focal Plane Arrays

Several solar-blind FPAs have also been successfully fabricated and tested. However, only a portion of these arrays were found to be active imagers, primarily due to the poorer quality of the $Al_xGa_{1-x}N$ materials containing higher aluminum mole fractions. In addition, to obtain UV images from a solar-blind array it is necessary that a solar-blind UV source be employed. In the present study, solar-blind UV images were obtained by using brass templates with geometric cutouts that were back-illuminated with the 253.6 nm line from a Hg(Ar) lamp and imaged with the UV FPAs. Figure [18] illustrates several solar-blind geometric images obtained using this technique.

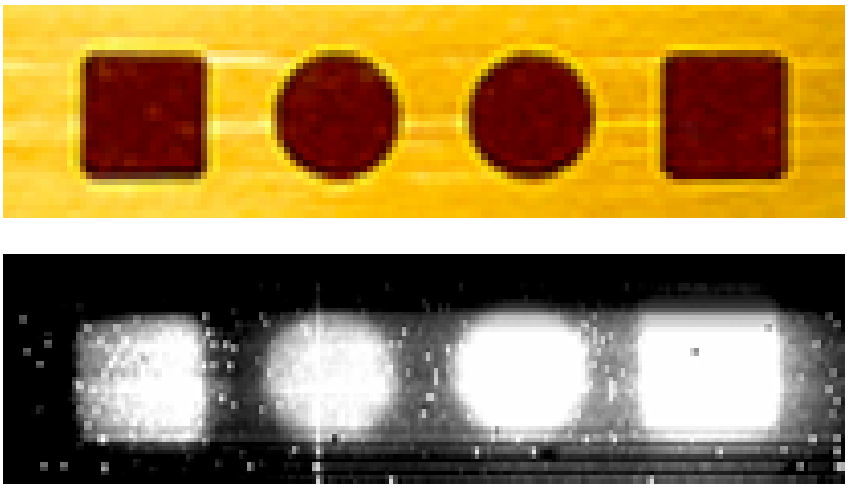

Figure 18: A visible image (top) and a UV image (bottom) of a brass template. The UV image was obtained with a 320x256 solar-blind FPA.

5.4 Improved 320x256 Visible-Blind Focal Plane Arrays

Extensive experiments were performed and designed in order to improve the quality of the 320x256 UV focal plane arrays. It was found through these experiments that pixel activation was being limited by the warping of the nitride-on sapphire samples used to

process the photodiode arrays. To circumvent this problem it was decided to increase the indium bump thickness from 5 μm to 10 μm on both the photodiode array and the silicon readout integrated circuit (ROIC) used in the hybridization process. This required the use of very thick photoresist (~15 μm thick) for the indium bump deposition process. However, deposition of thick photoresist on small samples (15 mm x 15 mm) was accompanied by severe edge bead problems. These edge beads prevented the photolithography process from being successfully completed for the very small diode bonding pads on both the diode array and the silicon ROIC. Indigo Systems, who produces and sells the silicon ROICs employed in this work, was contacted concerning this issue. When told that the samples were 15 mm x 15 mm squares, Indigo personnel indicated that they believed it impossible to deposit and use properly the very thick photoresist required for the deposition of 10 μm thick indium bumps due to the anticipated edge bead problem.

In spite of the formidable task described above, J. Matthews, a senior technician at NCSU, was able to perfect a process that minimizes the edge bead on small samples. This procedure took more than 200 experiments to perfect. Following this breakthrough, indium bump depositions and hybridizations were completed on three 320x256 visible blind UV focal plane arrays. This new procedure produced array that have a very high percentage of good pixels (greater than 95%).

A selection of UV images obtained using an improved 320x256 visible-blind nitride focal plane array are shown in Figures [19-23]. In Figure [19], a visible image of a standard television test pattern is shown alongside a UV image obtained through the back-illumination of a template (as described previously) and an improved 320x256 visible-blind FPA. It is seen from the figure that excellent detail is present in the UV image shown.

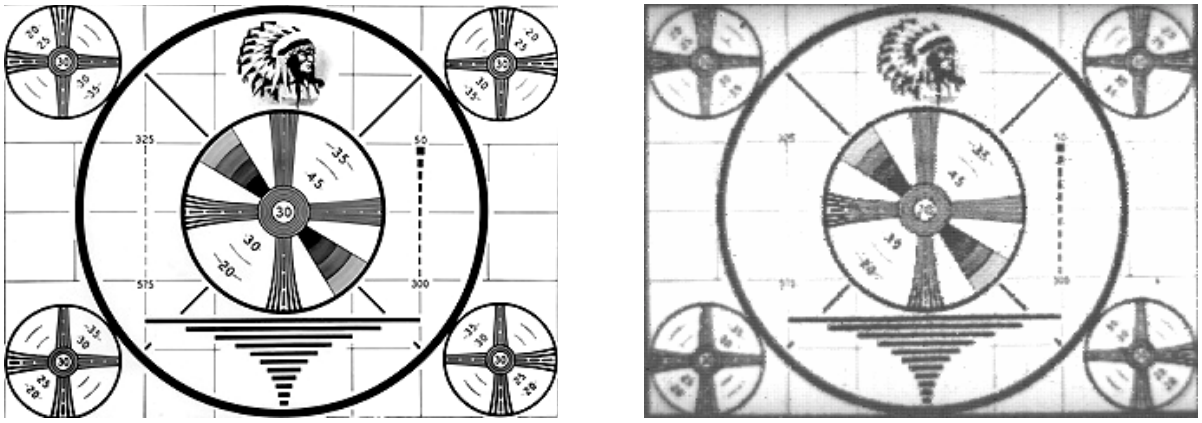

Figure 19: Visible (left) and UV (right) images of a standard television screen test pattern. The UV image was obtained with an improved 320x256 visible-blind FPA.

In Figure [20], a visible image of a standard brightness/contrast television screen test pattern is shown; next to this in the same figure is the UV image of the same test pattern. Again, excellent brightness and contrast ranges are present in the UV image shown.

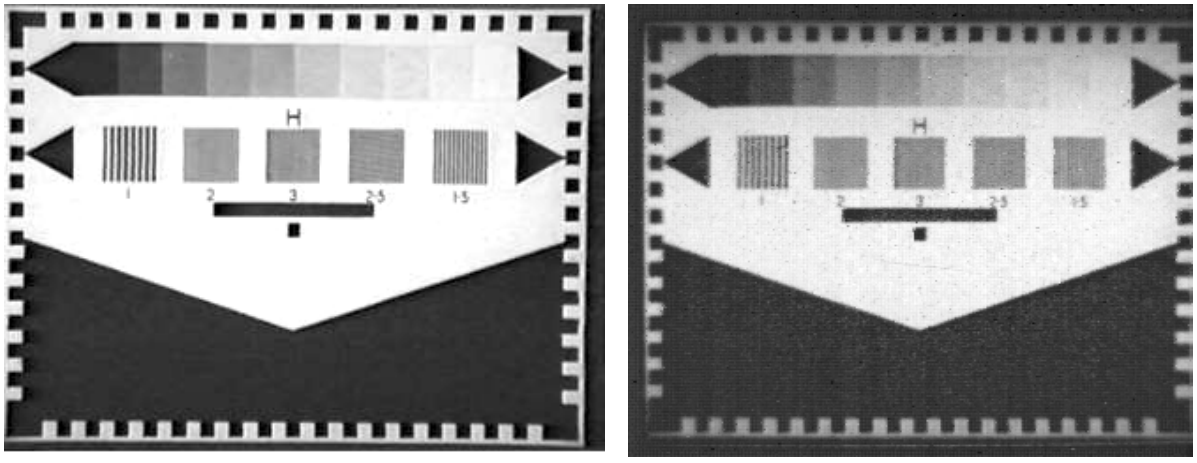

Figure 20: Visible (left) and UV (right) images of a standard brightness/contrast television screen test pattern. The UV image was obtained with an improved 320x256 visible-blind FPA.

In Figure [21], a visible image of the Engineering Graduate Research Center on the North Carolina State University campus is shown. Next to this in the same figure, the corresponding UV image obtained via the template technique described previously is shown. Note that excellent detail is present in the UV image.

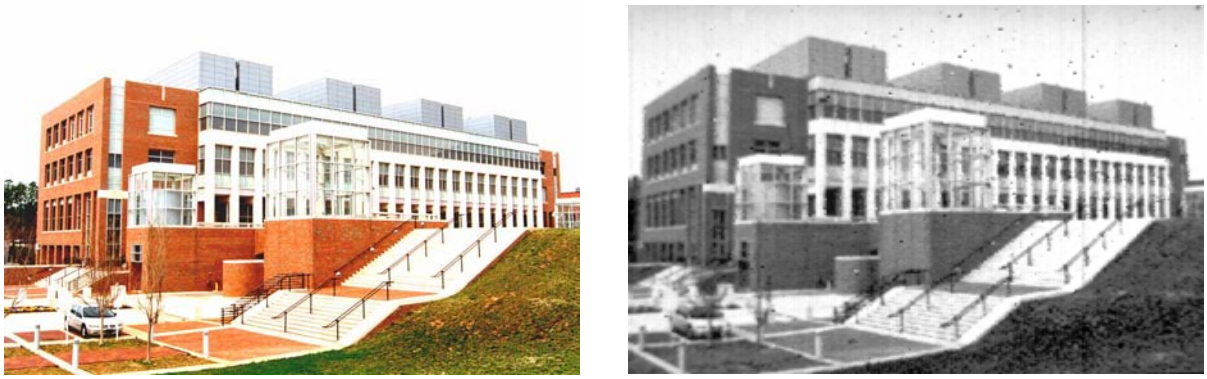

Figure 21: Visible (left) and UV (right) images of the Engineering and Graduate Research (EGRC) Building at North Carolina State University. The UV image was obtained with an improved 320x256 visible-blind FPA.

Figure [22] shows visible images of the same two individuals depicted in Figure [16]. Also shown are the corresponding UV images, obtained with an improved 320x256 visible-

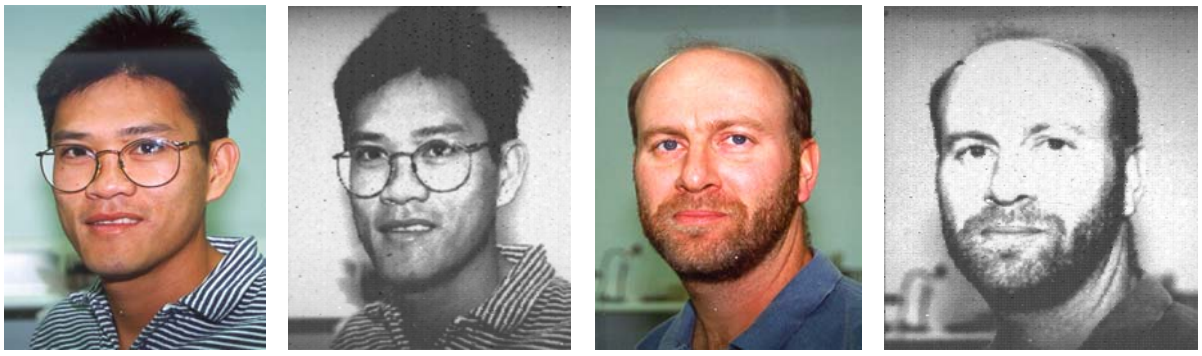

(a) (b) (c) (d)

Figure 22: Improved visible (a,c) and UV (b,d) images of the same two individuals depicted in Figure [16]. The UV images were obtained with an improved 320x256 visible-blind FPA.

blind FPA. Similar images of two other individuals are shown in Figure [23]. The

(a) (b) (c) (d)

Figure 23: Visible (a,c) and UV (b,d) images of two individuals. The UV images were obtained with an improved 320x256 visible-blind FPA.

improvement of the image quality with the use of 10 μm indium bumps is quite obvious. Also note, overall, the high percentage of active pixels in this UV image and the excellent brightness/contrast range exhibited in the image.

Figure [24] shows images of a complex vertical line spectrum. The images are from

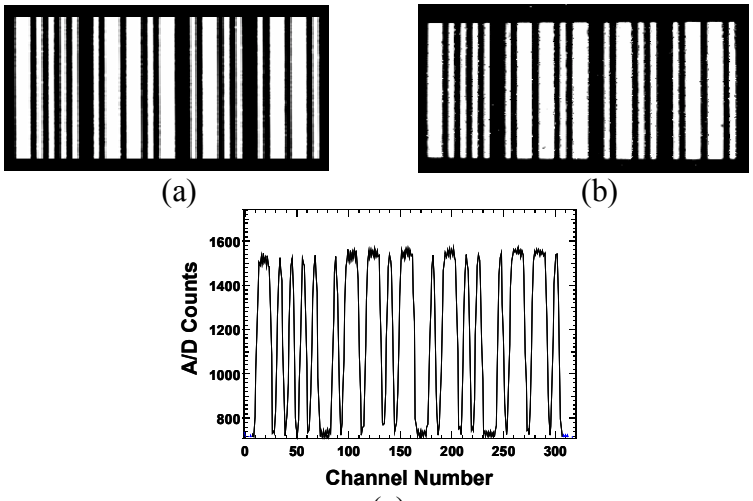

(a) (b) (c)

Figure 24: Visible (a) and UV (b) images of a vertical line spectrum. Also shown is a vertical channel scan. The UV image and the vertical channel scan both were obtained with an improved 320x256 visible-blind FPA.

a standard bar code in reality, but they could very well represent a complex optical emission spectrum in the UV. This type of image was chosen to illustrate both the UV imagery and channel scan capabilities of the 320x256 UV FPA. The first two images shown in Figures [24(a), 24(b)] are the visible and UV images of the bar code. The UV image was obtained with an improved 320x256 visible-blind FPA. Note that the UV image shows excellent reproducibility of the various lines shown in the visible image. In Figure [24(c)], a vertical channel scan from the 320x256 UV FPA is shown. In this case, the total photocurrent from each of the 256 vertical pixels associated with each of the 320 horizontal channels has been summed under hardware and software control and then displayed as a vertical channel spectrum. This illustrates that the new 320x256 visible-blind UV FPAs may find use as a fast 320-channel solid-state UV detector array when used as the output detector for UV spectrometer, for example. The 300-365 nm UV wavelength region is particularly important for the fluorescence spectroscopy of bio-agents such as anthrax and other biomaterials containing tryptophan.

Histograms for the pixel distributions of the dark current noise I_{DK}, the photocurrent $I_{PH,}$, the noise equivalent power NEP, and the detectivity D* were obtained for selected 320x256 visible-blind hybridized arrays using the SE-IR FPA evaluation software. Results of these studies are shown in Figures [25, 26] for a representative 320x256 visible-blind FPA. It should be noted that the Indigo 9809 ROIC employed comes equipped with a capacitance trans-impedance amplifier (CTIA) input stage as a noise-reduction feature. The hybridized FPA histograms reflect the combined noise characteristics of both the silicon ROIC and the nitride photodiode array.

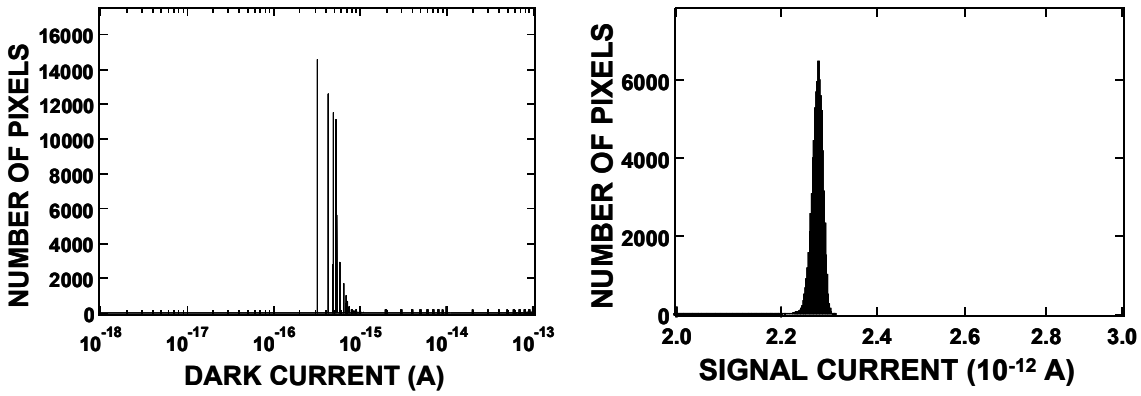

Figure 25: Histograms showing the output currents from the hybridized UV FPA under no illumination (left) and under a uniform illumination (right).

Figure [25(a)] shows the distribution of dark noise currents. It is seen that a large majority of the FPA pixels exhibit very low dark currents in the range of 3-7 x 10^{-16} A. Under a moderate uniform UV illumination, the FPA shows excellent pixel photocurrent uniformity, as illustrated by the narrow FWHM of the peak in Figure [25(b)]. Note that this peak is centered at about 2.26 x 10^{-12} A for the illumination intensity employed. This gives a signal-to-noise ratio of about 4-5 x 10^{3} for this particular level of illumination.

Using the data shown in Figure [25(a)], along with Equations (8) and (12), histograms for the noise equivalent power (NEP) and for the detectivity D* were obtained for selected 320x256 FPAs. Representative histograms are shown in Figure [26]. It is seen that the pixel noise equivalent power forms a tight distribution peaked at about 2 x 10^{-15} A. This corresponds to a distribution of detectivities peaked at about 1 x 10^{13} cmHz$^{1/2}$W^{-1}, as shown in Figure [26(b)].

These results all emphasize the very low noise and very high sensitivity exhibited by the visible-blind nitride UV FPAs.

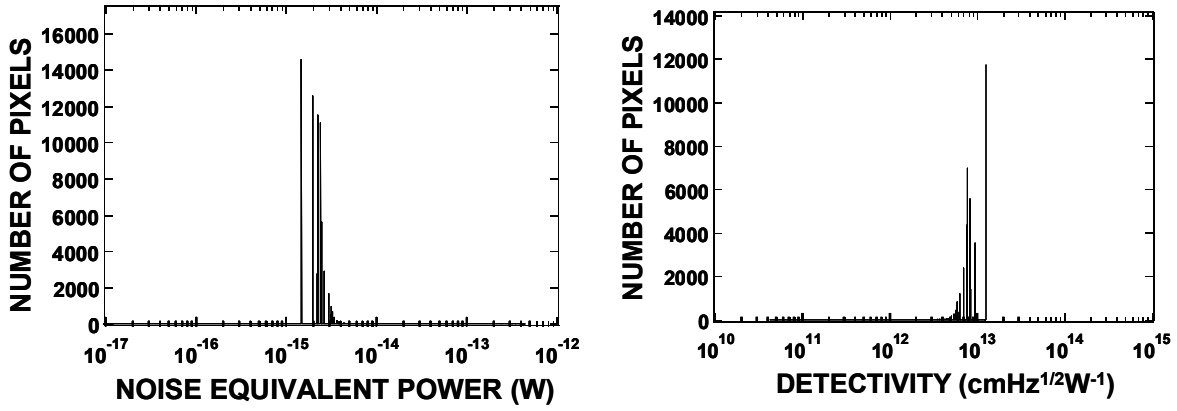

Figure 26: Histograms showing the noise equivalent power (left) and the detectivity (right) from the hybridized UV FPA.

5.5 Testing at the Night Vision Laboratories

Both 128x128 and 320x256 visible-blind UV focal plane arrays were used during the small arms firing experiments conducted at the Night Vision Laboratory at Fort Belvoir on March 1, 2002. The SE-IR camera, equipped with several different UV FPAs, was used to image the firing of two different small arms, an M16 assault rifle and an M24 sniper rifle.

Figure [27] shows photos of a U.S. Army Sergeant preparing to fire an M16 rifle as part of the testing. In several initial test firings of this weapon prior to digital recording of

Figure 27: A photograph of the set-up used for testing at the Night Vision Laboratories at Fort Belvoir.

the firing event with the NCSU UV digital camera, it was noted that the M16 rifle was equipped with a flash suppressor at the end of the rifle barrel such that the only visible light emitted during firing appeared to be a very dim, deep-red flash. When this rifle flash was observed with the UV camera running, there was no UV signature found, aside from a very brief reaction that was attributed to the sonic shockwave from the rifle rather than from UV emission. In view of the visual observation of the flash, it is felt that the M16 rifle equipped with a flash suppressor contained little or no UV component of the flash emission spectrum. When we asked NVL personnel what the emission spectrum was like for the M16 rifle, no one involved with the testing could answer this question. Figure [28] shows a close-up view of the flash suppressor on the barrel end of the second weapon used in these tests, an M24 sniper rifle.

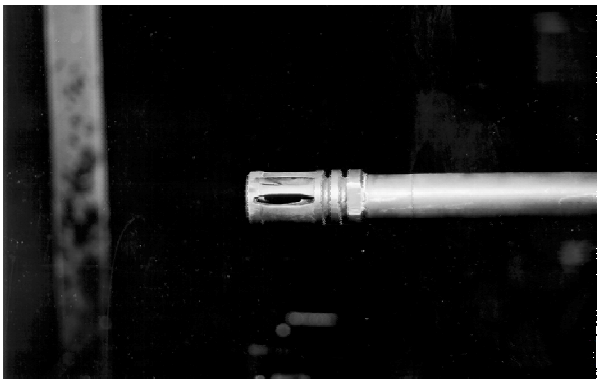

Figure 28: A close-up view of the flash suppressor on an M24 sniper rifle. The flash suppressor for the M16 was similar.

Initial test firing of the M24 sniper rifle indicated that, much like the M16 rifle, the only visible light emitted during firing appeared to be a very dim, deep-red flash. When the firing rifle flash from the sniper rifle was observed with the UV camera running, again, there

was no UV signature found other than a very brief reaction that was attributed to the sonic shockwave from the rifle rather than from UV emission. This null result is similar to the result found for the M16 rifle fire.

On the basis of these test, it is unlikely that the visible-blind or solar-blind UV FPAs can be used to detect small weapons activities, or in fact to detect any radiation which has such a small tail in the UV region of its blackbody spectrum.

6. SUMMARY AND CONCLUSIONS

The successful development of both discrete UV photodiodes and large-format UV imaging arrays consisting of 128x128 and 320x256 AlGaN p-i-n photodiodes is reported. These devices exhibit very low noise and very high sensitivity to UV radiation. Excellent quality UV images have been obtained for both 128x128 and 320x256 large format hybridized FPAs. These new devices may find widespread usage in a number of applications that require sensitive UV detectors and UV imagers but where the cost, size, and power requirements of a photomultiplier tube cannot be justified.

REFERENCES

[1] See, for example, IR digital cameras that are available from Indigo Systems (http://www.indigosystems.com).

[2] B.F. Levine, “Quantum well infrared photodetectors”, J. Appl. Phys. 74 (8), R1 (1993).

[3] M.A. Gadir, P. Harrison, R.A. Soref, “Responsivity of quantum well infrared photodetectors at terahertz detection wavelengths”, J. Appl Phys. 91 (9), 5820 (2002).

[4] C.E. Kolb, S.B. Ryali, and J.C. Wormhoudt, "The Chemical Physics of Ultraviolet Plume Signatures", SPIE Conference Proceedings 932, 2 (1988).

[5] Hadis Morkoc, "GaN-Based Modulation-Doped FETs and UV Detectors", Naval Research Reviews 51(1), 26 (1999).

[6] Dennis K. Wickenden, Zhenchun Huang, D. Brent Mott, and Peter K. Shu, "Development of Gallium Nitride Photoconductive Detectors", Johns Hopkins APL Technical Digest **18(2)**, 217 (1997).

[7] Wei Yang, Thomas Novova, Subash Krishnankutty, Robert Torreano, Scott McPherson, Holly Marsh, "Back-illuminated GaN/AlGaN heterojunction photodiodes with high quantum efficiency and low noise", Appl. Phys. Lett. 73(8), 1086 (1998).

[8] T. Huang, D.B. Mott, A. La, "Development of 256x256 ultraviolet imaging arrays", SPIE Conference Proceedings **3765**, 254 (1999).

[9] J.D. Brown, J. Matthews, S. Harney, J. Boney, J.F. Schetzina, J.D. Benson, K.V. Dang, Thomas Nohava, Wei Yang, and Subash Krishnankutty, "Visible-Blind UV Digital Camera Based on a 32 x 32 Array of GaN/AlGaN p-i-n Photodiodes", MRS Internet J. Nitride Semicond. Res. **4**, 9 (1999).

[10] J. D. Brown, J. Matthews, S. Harney, J. C. Boney, J. F. Schetzina, J. D. Benson, K. V. Dang, Thomas Nohava, Wei Yang, Subash Krishnankutty, "High-Sensitivity Visible-Blind AlGaN Photodiodes and Photodiode Arrays", MRS Internet J. Nitride Semicond. Res. **5S1**, W1.9 (2000).

[11] J.D. Brown, J. Boney, J. Matthews, P. Srinivasan, J.F. Schetzina, Thomas Nohava, Wei Yang, Subash Krishnankutty, "UV-Specific (320-365 nm) Digital Camera Based On a 128x128 Focal Plane Array of GaN/AlGaN p-i-n Photodiodes", MRS Internet J. Nitride Semicond. Res. **5**, 6 (2000).

[12] D. Walker, V. Jumar, K. Mi, P. Kung, X.H. Zhang, and M. Razeghi, "Solar-Blind AlGaN Photodiodes with Very Low Cutoff Wavelength", Appl. Phys. Lett. **76**, 403 (2000).

[13] E.L. Tarsa, P. Kozodoy, J. Ibbetson, and B.P. Keller, "Solar-Blind AlGaN-Based Inverted Heterostructure Photodiodes", Appl. Phys. Lett. **77**, 316 (2000).

[14] After Dr. R.M. Kolbas (unpublished work).

[15] S.M. Sze, Physics of Semiconductor Devices, Wiley, New York (1981).

[16] S.L. Chuang, Physics of Optoelectronic Devices, Wiley, New York (1995).

[17] The Book of Photon Tools, p. 1-25, distributed by Oriel Corporation (http://www.oriel.com).

[18] H. Morkoç, Nitride Semiconductors and Devices, Springer, New York (1999).